Manuscript #4664, Revision 1

Quantification of α-particle radiation damage in zircon

Katie M. Smye[1,*], Clive Brigden[1], Eric R. Vance[2] and Ian Farnan[1]

[1]Department of Earth Sciences, University of Cambridge, Downing Street, Cambridge CB2 3EQ, U.K.

[2]Institute of Materials Engineering, Australian Nuclear Science and Technology Organisation, Lucas Heights, Menai, New South Wales 2234, Australia

*E-mail: katie.smye@beg.utexas.edu

Current address: Bureau of Economic Geology, University of Texas at Austin, University Station, Box X, Austin, TX, U.S. 78713

Abstract

Analysis of radiation damage in natural mineral analogues such as zircon is important for the evaluation of the long-term behavior of nuclear waste forms and for geochronology. Here we present results of experiments to determine the partitioning of radiation damage due to the heavy nuclear recoil of uranium and thorium daughters and the α-particles ejected in an α-decay event in zircon. Synthetic polycrystalline zircon ceramics were doped with ^{10}B and irradiated in a slow neutron flux for 1, 10, and 28 days to achieve the reaction $^{10}B + n \rightarrow {}^{7}Li + \alpha$ (+2.79 MeV), creating an alpha event without a heavy nuclear recoil. The ^{7}Li atoms produced in the nuclear reaction were directly detected by NMR 'spin-counting', providing a precise measurement of the α-dose applied to each sample. The amount of damage (number fraction and volume fraction) created by each α-event (one α-event being a ^{7}Li + α-particle) has been quantified using radiological nuclear magnetic resonance and X-ray diffraction data. The number of permanently displaced atoms in the amorphous fraction was determined by ^{29}Si NMR to be 252 ± 24 atoms for the $^{10}B(n,\alpha)$ event when the heavy recoil is absent, which is broadly in agreement with

ballistic Monte Carlo calculations. The unit cell swelling of the crystalline fraction, determined by X-ray diffraction, is small and anisotropic. The anisotropy is similar to that observed in ancient natural samples and implies an initial anisotropic swelling mechanism rather than an anisotropic recovery mechanism occurring over geological time scales. The small unit cell volume swelling is only ~6% of the expansion frequently attributed to α-particles associated with an actinide α-decay event. The lattice parameters indicate a volume increase as a function of alpha dose of 0.21 $A^3/10^{18}$ α-events/g, which is significantly less than the increase of 3.55 $A^3/10^{18}$ α-events/g seen in Pu-doped zircon and 2.18 $A^3/10^{18}$ α-events/g seen in natural zircon. It is concluded that the heavy recoil plays a more important role in unit cell swelling than previously predicted. The likely mechanism for such an effect is the rapid, and thus defect-rich, recrystallization of material initially displaced by the heavy recoil.

Keywords: zircon, NMR spectroscopy, radiation damage, α-particle

Introduction

Radiation damage in zircon is important as a natural analogue study of the behavior of nuclear waste forms over geological time periods. Zircon has a high critical amorphization temperature (Meldrum et al. 1999), which means that the structures of ancient zircons preserve, rather than recover, most of the structural disruption that occurs during alpha decay or spontaneous nuclear fission of actinides incorporated in the lattice. Thus, it records the scale of disruption cause by the alpha decay of actinides, which will be the dominant damage mechanism in spent nuclear fuel and actinide nuclear waste form materials beyond about 500 years after emplacement in a geological repository (Bruno and Ewing 2006, Hedin 1997). The damage caused by alpha emitters is comprised of damage from the recoil of the heavy alpha-emitting

nucleus (~70 – 100 keV) and the α-particle itself (~4.5 – 5.5 MeV) when the actinides uranium and thorium (and α-emitting daughters) undergo α-decay events that damage mineral structures over geological time. The response of zircon in nature is swelling and a loss of crystallinity exemplified by the seminal study by Holland and Gottfried (1955) and subsequent work (Murakami et al. 1991, Palenik et al. 2003). Zircon exposed to ion beam-induced damage (Wang and Ewing 1992, Weber et al. 1994) and plutonium doping (Weber 1990) also exhibits similar behavior. Both the crystalline and amorphous regions of the zircon swell as a result of alpha radiation damage. To date, there has been no experimental measure of the partitioning of the structural damage between alpha particle and heavy recoil and the effects of these two processes on swelling in the partially crystalline zircon in bulk materials. Such a measurement tests our understanding of the radiation damage process that applies more widely in other actinide-containing minerals and nuclear materials. Radiological nuclear magnetic resonance (NMR) and X-ray diffraction (XRD) measurements have been applied to quantify the damage created by light, highly-energetic particles generated by the nuclear reaction: $^{10}B + n^{o} \rightarrow {}^{7}Li + \alpha$ (+2.79 MeV, 2.31 MeV kinetic energy) (Figure 1), on the crystalline structure of a synthetic zircon ceramic. This nuclear reaction involves only light particles and thus eliminates the heavy recoil component of the actinide alpha-decay process.

The ^{7}Li nuclear reaction product is NMR active, and is the only source of ^{7}Li in the sample. Because signal intensity in NMR is directly proportional to the number of nuclei present, 'spin-counting' can used to provide a very precise measure of dose – a precision not achieved by standard dose calculations based on average neutron fluence and a small boron mass fraction (0.3 wt%) in the sample – by directly detecting the ^{7}Li nuclear reaction product and comparing to a calibration curve relating the signal to the number of ^{7}Li atoms present.

In order to acquire a complete picture of the damage created by the α-events, both XRD and ^{29}Si NMR are used. X-ray diffraction is useful for understanding the long-range order in a material and the nature of crystalline regions including changes in lattice parameters, strain, and disorder. However, while it may provide information about the *presence* of amorphous regions, it is less useful for studying their *nature*. On the other hand, NMR can be applied to both amorphous and crystalline materials and is very sensitive to changes in the local structural environment of atoms. It probes changes on small length scales, generally within one or two coordination spheres around the nuclei being probed. Furthermore, because NMR utilizes the permanent nuclear dipole present in each nucleus being probed, the intensities in a spectrum are directly proportional to the number of atoms in a specific phase. In this study, the effects from solely α-particle and ^{7}Li damage are compared with previous studies on damage created by α-particle + heavy recoil events in natural and Pu-doped zircons. We identify both of these processes as α-events. However, actinide alpha emission consists of an alpha particle with a μm-scale range together with a heavy daughter recoil with a range of ~20 nm, while the ^{10}B(n,α) alpha emission consist of two light particles (α-particle and ^{7}Li), both with ranges of the order of microns.

The zircon structure is tetragonal ($I4_1/amd$, Z = 4) and consists of chains of alternating, edge sharing ZrO_8 dodecahedra and SiO_4 tetrahedra along the *c*-axis. There is one Zr-Si distance along the chain, and two (×4) unique Zr-O bond distances (Ni et al. 1995). Each O atom is coordinated to one Si atom and two Zr atoms. The zircon structure accommodates heavier rare-earth elements, and Y and Sc, whereas the closely related monazite-type monoclinic structure accommodates lighter, larger REEs. The zirconium (IV) site is a host for many actinides and other elements. Natural samples often contain U and Th in concentrations of 5,000 ppm, and up

to 10 wt% actinides has been observed. Plutonium has been shown to be at least 8.85 wt% soluble in synthetic zircon samples (Weber 1990).

Radiation damage in zircon has been widely studied both for its application in geochronological studies and its usefulness as a potential nuclear waste form. Earlier studies report up to 18% total volume swelling (e.g. Holland and Gottfried 1955, Weber et al. 1998), which is a combination of swelling of the crystalline lattice and the formation of amorphous regions. Unit cell volume swelling of up to 5% at 5.8×10^{18} α-events/g is observed in natural zircon (Holland and Gottfried 1955, Murakami et al. 1991), and is anisotropic with a maximum swelling of 1.5% along *a* and 2% along *c*. Rios et al. (2000a) propose that the anisotropy in radiation-induced lattice swelling could be either the result of anisotropy in expansion of the ZrO_8 polyhedra or preferential relaxation along the *a*-axis on geological timescales. The anisotropy is more pronounced in natural studies than in Pu-doped studies (Weber 1993).

In the early stages of amorphization in zircon ($<3 \times 10^{18}$ α-events/g), previous workers have attributed the unit-cell expansion in radiation-damaged zircon to localized defects caused by α-particles (Marples et al. 1970, Rios and Salje 1999). The damage geometry has been described as largely isolated regions of displaced atoms along the long track (Matzke 2007) with spatial separation on the order of microns. Monte Carlo calculations on ^{239}Pu-doped zircon give ~220 atoms displaced per α-particle (Weber 1998). However, the disposition of the displaced atoms is poorly understood.

Amorphous regions constitute the minority phase at low levels of damage, and are formed primarily by the lower energy, heavy ions from Pu or actinide α-recoil which travel tens of nanometers in zircon and lose most of their energy through collisions with other atoms in the sample. The cascades are ~50 Å diameter (Weber et al. 1994), and are thought to be a contiguous

region of many displaced atoms (Salje et al. 1999, Sickafus 2008). Amorphization due to α-decay in zircon has previously been investigated by NMR. Results show that the silicate tetrahedra tend to polymerize, with bridging oxygen atoms connecting tetrahedra (Farnan and Salje 2001, Ashbrook & Farnan 2004, Farnan et al. 2007).

Materials and Methods

Sample Preparation and Characterization

Polycrystalline zircon samples were synthesized from Zirconium (IV) t-Butoxide ($Zr(OC_4H_9)_4$) mixed with Ludox® (40 wt% SiO_2 colloidal suspension) and 0.4 wt% H_3BO_3 (with ^{10}B in natural abundance of 19.9 %). The low B content was chosen to achieve significant damage but minimize in-reactor sample heating (see next section). Additional water and ammonia (NH_3) were added to reach approximately pH 9. The mixture was stir-dried, calcined in air at 750°C, wet ball-milled, dried, and hot isostatically pressed (HIPed) at 1300 °C and 100 MPa for three hours. X-ray diffraction showed phase-pure crystalline zircon; however, scanning electron microscopy (SEM) imaging showed a small amount of zirconia (ZrO_2) (Figures 2a and 2b). The sample was reheated at 1500°C for five hours, and total weight loss during the sintering heat treatment was approximately 2%.

As boron is unable to substitute into the zircon structure, it was determined that it must be present as an internal coating of the sample pores as borosilicate or borate glass. ^{11}B MASNMR spectra show boron present in three- and four-fold coordination with oxygen in a disordered phase, which is consistent with this interpretation.

Sample Irradiation

The samples were irradiated for 1, 10, and 28 days in a flux of thermal neutrons (5×10^{13} n/cm^2s) at the HIFAR reactor, Australian Nuclear Science and Technology Organisation

(ANSTO), to achieve the reaction $^{10}B + n^o \rightarrow {}^7Li + \alpha$. Samples were subjected to a total neutron fluence of 4.3×10^{18} n/ cm^2, 4.3×10^{19} n/ cm^2, and 1.2×10^{20} n/ cm^2, respectively.

The sample temperature due to radiogenic heating was calculated to be approximately 150 °C during the 28-day irradiation, which is considerably below the temperature at which radiation damaged zircon will anneal (e.g. Zhang et al. 2000, Geisler et al. 2001) and its critical amorphization temperature determined by ion beam studies (Meldrum et al. 1999). Annealing studies of He ion-implanted $ZrSiO_4$ waveguides report some mobility of isolated defects toward larger defect clusters upon heating between 100 – 200 °C, but no recovery of amorphized regions and no decrease in the total number of defects up to 1000 °C (Babsail et al. 1991). Because the samples were activated upon irradiation, they could not be handled outside a radiologically controlled area for several years. The 28-day sample had a residual radioactivity level of 1000 μSv/hr at contact during analysis.

Pore size determination.

In order to determine the proportion of ^{7}Li and α-particles that exit the glassy pores and cause damage in the crystal structure, it is necessary to calculate the probability of boron being in a given pore with radius *r* and, using the most likely pore radius, determine whether or not ^{7}Li and α-particles will escape. This requires measurement of the average pore diameter and scaling for volume to account for a greater proportion of boron being contained in larger pores.

Scanning electron microscopy images were analyzed in ImageJ software (Rasband 1997-2001). A threshold was applied to isolate dark regions (pores) from the zircon ($ZrSiO_4$) and minor zirconia (ZrO_2) phases (Figure 3a). Then, pore sizes of greater than 0.005 μm^2 were selected (providing over 7000 points) and fit to ellipses to provide major and minor axes lengths

(Figure 3b). The resulting data were plotted as a histogram with 50 bins of radius length up to 4.2 μm^2 (Figure 4a).

A Jacobian transformation (Equation 1) was used to find the pore volume distribution, G(V), of boron in a pore of radius *r* as a function of the distribution of pore radii, g(r), to account for more boron being contained in larger pores:

$$G(V) = g(r)\frac{\partial V}{\partial r} \quad (1)$$

A bin radius was squared, and multiplied by the frequency of the bin, providing the probability of boron being in any given pore of radius *r*. The results were plotted and fitted to a Gaussian peak profile to provide the most probable pore radius to contain boron (Figure 4b). This approach is valid despite the possibility of 10B being present as a coating of the larger pores, and despite a large proportion of the reaction productions (^{7}Li and α-particle) needing to travel across the pore to enter the zircon sample. The range of an alpha particle in air is several centimeters and so this will not impede the particles' entry into the sample. A filled glass pore would represent a worst-case scenario for the range of energetic light particles produced from the ^{10}B(n,α) reaction.

TRIM Simulations

Ballistic Monte Carlo simulations using the TRIM software (Ziegler et al. 2010) were carried out to determine the penetration of the ^{7}Li and the α-particles into the synthetic zircon ceramic. The calculations consisted of 100,000 ^{4}He (1.47 MeV) or ^{7}Li (0.84 MeV) atoms projected into a two-layer target of borosilicate glass of density 2.5 g/cm^3 (thickness, 1.0 μm) and $ZrSiO_4$ with a density of 4.67 g/cm^3. Displacement energies used were 89 eV (Zr), 48 eV (Si), and 28 eV (O) (Park et al. 2001). The sum of all trajectories is shown in Figure 5a.

Numbers of displaced atoms/vacancies created by each trajectory are tracked by the software and reported as the average number of vacancies over the simulation.

^{7}Li MAS-NMR.

A calibration curve was constructed using micromolar quantities of spodumene ($LiAlSi_2O_6$), which was chosen because it has a well-defined stoichiometry and a small mass fraction of ^{7}Li, allowing us to use measurable quantities for calibration. Samples ranging from 0.25 to 2.5 mg spodumene (6.6×10^{17} to 7.35×10^{18} ^{7}Li atoms, using ^{7}Li natural abundance of 92.4%) were weighed using a microbalance (±0.5 μg). The spodumene crystals were loaded into rotors with alumina powder to secure their position in the center of the rotor and NMR coil. Lithium-7 MAS-NMR spectra were acquired for each spodumene sample using a Varian Infinity Plus 500 MHz NMR spectrometer (11.7 T) operating at 194.24 MHz. Samples were spun at 10 kHz. In most cases, 24 scans were acquired; however, if more scans were needed to increase the signal to noise ratio, spectra were normalized to 24 scans. Spectra were acquired with a 1 μs pulse width ($\pi/6$) and 300 s pulse delay to ensure complete relaxation between scans. Each spodumene sample was run at least three times over the span of several weeks to determine the error in spectrometer sensitivity given similar tuning conditions. The spin of the ^{7}Li nucleus is 3/2; the sharp peak at -8.6 ppm due to the central (½ - ½) NMR transition was integrated to determine the signal produced for each 10^{18} ^{7}Li atoms present. Zircon ^{7}Li NMR spectra were acquired using the same experimental parameters as spodumene, and were referenced to spodumene at 0.8 ppm.

Radiological MAS NMR

Because sample impurities were activated (primarily to ^{60}Co) upon irradiation, samples were stored on-site at ANSTO for several years before analysis. Dose measurement at contact was up to 1000 μSv/hr for the 28-day irradiation. Upon transfer to the University of Cambridge, the powdered zircon samples were removed from transport containers and transferred to a glove bag. A portion of the powder from each irradiation was removed from the irradiation container and inserted into a PTFE liner by first placing the liner in a PTFE holder, inserting a funnel, and dropping in the powder without contaminating the screw thread or the outside of the container. A PTFE cap was screwed on, and the entire liner assembly was placed in a 7.5 mm zirconia rotor. Swabbing for transferable contamination was carried out at each stage of filling for the primary and secondary containment.

^{29}Si MAS NMR.

^{29}Si spectra of undamaged and damaged zircon were acquired using a Varian Chemagnetics Infinity 400 MHz (9.4 T) spectrometer operating at 79.47 MHz for ^{29}Si, and were secondary referenced to TMS (tetramethyl silane) using RTV silicone rubber at -22.3 ppm. The low natural isotopic abundance of ^{29}Si (4.7%) and very long T_1 relaxation time make it difficult and time-consuming to acquire a spectrum with good signal-to-noise ratio. To obtain a spectrum in a reasonable amount of time, we used a rotor-synchronized Carr-Purcell Meiboom-Gill (CPMG) echo technique, which has been shown to provide a good representation of the of the single-pulse ^{29}Si lineshape on natural zircon with long relaxation time components (Larsen and Farnan 2002). An echo train is collected following a long polarization period of 3600 seconds. For each sample, 64 spin-echoes were acquired with a 90˚ pulse width of 3.7 μs and a 180˚ pulse width of 7.3 μs with the sample spinning speed at 5.188 kHz. The pulse spacings of 25 ms give intrinsic CPMG resolution of 40 Hz. The echoes were added together to create a composite

whole echo, and a magnitude Fourier-transform was applied to avoid the need to phase-correct the spectrum. For unirradiated zircon, the CPMG method was not suitable due to the width of the echo in the time domain (narrow line, wide echo). In this case, the unirradiated spectrum was collected using a Bloch decay with 8 acquisitions ($\pi/10$) and a 100 s pulse delay.

The fraction of Si atoms in each of the amorphous and crystalline phases can be found by deconvolution of the spectra into crystalline (sharp peak) and amorphous (broad area) fractions. The amorphous fraction, f_a, was determined by fitting the sharp crystalline peak in the spectrum to a Lorentzian peak profile, and constraining the broad amorphous region using a Gaussian peak profile. The area of the main peak was then subtracted from the integration of the whole spectrum to provide the proportion of Si atoms in the amorphous phase.

X-ray diffraction

Sample preparation for X-ray diffraction analysis was carried out in a sealed glove bag to avoid dispersion of particles. For each sample, ~ 60 mg powder was placed onto a glass cover slip mounted to a sample holder. A 1:3 mixture of durafix glue and water was dropped onto the cover slip and mixed with the sample to ensure that the powder would not be dispersed during analysis. Samples were analyzed on a Bruker D8 diffractometer using Cu $K_{\alpha 1}$ radiation, a 0.01° step size from 10 to 100° 2Θ, and counting times of 5 (unirradiated), 10 (1-day), 22.5 (10-day), and 45 seconds (28-day). The unirradiated sample was run with and without the glue preparation method to observe the effects of the glue on the diffraction pattern. Powder diffraction patterns were analyzed using least-squares refinement per the Rietveld method (Rietveld 1969) in the General Structural Analysis System (GSAS) software (Larson and Von Dreele 2004) with the graphical user interface EXPGUI (Toby 2001). The peak intensities were normalized to the glue

background, and patterns were refined to find changes in lattice parameters, peak intensities, and broadening.

Results

Fate of ^{7}Li and α-particles

Based on image analysis and pore-size determination, the average boron-containing pore diameter was calculated to be 1.2 μm. Ion range calculations show that the α-particles of the ^{10}B(n, α) reaction have enough energy to escape from the pore regions and penetrate at least 4 μm into the zircon ceramic (Figure 5a) (as do the 0.84 MeV ^{7}Li atoms, track length 2 μm.)

The range and energy of particles produced in the ^{10}B(n, α) reaction is important for the comparison of naturally- and synthetically-damaged samples. The ^{10}B (n, α) energy of 2.79 MeV is significantly less than an alpha particle arising from the ^{238}U alpha decay (4.198 MeV). A priori, this would be thought to result in less structural damage being created by the two light particles where the energy is partitioned as 1.47 MeV for the α-particle and 0.84 MeV for ^{7}Li. However, the majority of the atomic displacements occur at the end of the particle track when nuclear, rather than electronic, stopping becomes the primary interaction mechanism. Thus, an increase in the total energy of a particle tends to increase the range in the solid rather than the total number of atoms displaced. Figure 5b compares the energy loss profiles of 4.198 MeV and 1.47 MeV α-particles. If the lower energy profile is shifted in penetration depth, the profiles are almost perfectly superimposable. This final part of the track is responsible for the majority of atomic displacements and the code (Ziegler et al. 2010), predicts that a 4.198 MeV α-particle should create 89 vacancies/ion along its 10.7 μm track through $ZrSiO_4$ compared with 73 vacancies for the 4 μm 1.47 MeV α-particle track. This predicts about 65 displaced atoms associated with the end of the α-particle track, assuming a linear number of displacements with

track length at energies well above the Bragg peak. These simulations indicate that ~83% of the damage created by the α-particle emitted in an actinide α-decay should be reproduced by the lower-energy α-particle from the $^{10}B(n, \alpha)$ reaction.

^{7}Li calibration

Calibration of the ^{7}Li signal produced by each ^{7}Li atom in spodumene is shown in Figure 6. The ^{7}Li signal in the zircon samples was quantified by integration of the central ($^{1}/_{2} - {}^{1}/_{2}$) NMR transition, which is unaffected by first order quadrupolar interactions. Figure 7 shows a representative spectrum from the 28 day sample. Results for the dose calculations are shown in Table 1. For each irradiated sample, the integrated ^{7}Li spectrum is calibrated to a precise number of ^{7}Li atoms, and each ^{7}Li is the result of one α-event. The number of α-events created in each irradiated sample is converted to α-events/g based on the sample mass analyzed by NMR. The signal observed from the highest neutron fluence applied to the samples yields 20.4 (±3.1) × 10^{18} ^{7}Li atoms/g and hence 20.4 × 10^{18} α-events/g. This exceeds the α-dose required to completely amorphize zircon by both natural actinide α-decay, (8—10 × 10^{18} α/g [Holland and Gottfried 1955, Murakami 1991, Rios et al. 2000b]) and Pu-doping (6.7 × 10^{18} α /g [Weber et al. 1994]).

^{29}Si MAS-NMR

The effect on the silicon local environment in zircon of the deposition of energy from the ^{7}Li and α-particles created in the neutron-induced nuclear reaction can be observed via the ^{29}Si NMR spectra shown in Figure 8a. The narrow, symmetric peak at -81.6 ppm corresponds to Si atoms bonded to the four non-bridging oxygen atoms of isolated SiO_4 tetrahedra in the undamaged zircon structure (Magi et al. 1984). With increasing dose, an additional broad resonance at more negative chemical shifts is observed. These spectra are similar to previous NMR studies on radiation-damaged natural zircon (Farnan and Salje 2001, Farnan et al. 2007)

where the broadening of the main peak was attributed to defects within the crystalline lattice and the broad resonance at more negative chemical shifts was due to the formation of amorphous regions associated with heavy recoil. An example of the deconvolution of the spectra into crystalline (sharp peak) and amorphous (broad area) fractions can be found in Figure 8b. The amorphous fraction increases with cumulative dose, and reaches 23% at a cumulative dose (D_α) of 6.3 (±1.0) × 10^{-3} α-events/Si atom (Figure 9). The intensity of the NMR signal is directly proportional to atomic abundance, and so provides the amorphous number fraction, f_a, (in proportion of Si atoms in the amorphous phase) associated with the ^{7}Li and α-particle tracks. When radiation damage accumulates directly, the damage fraction will initially increase linearly with dose. As the total dose increases and damaged volumes build up, subsequent events will create a smaller damaged volume per event as some affected atoms will already have been displaced. This behavior has been described in the literature by Gibbons (1972) for ion-beam experiments and by Marples (1988) for α-doping experiments. The direct accumulation of damage equation (Equation 2) similarly describes the fraction of displaced atoms using the number of α-events/Si atom scale, D_α known from the ^{7}Li content, f_a can be fitted to a direct damage equation:

$$f_a = 1 \quad \exp(\ N_d D\ ) \tag{2}$$

and the number of Si atoms displaced in each α-event, N_d, may be determined. This yields 42 ± 4 Si atoms displaced per α-event, which corresponds to 252 ± 24 total atomic displacements per event.

X-ray diffraction

X-ray diffraction of damaged zircon samples show a shift in Bragg peaks to lower 2Θ, a decrease in peak intensity, and an increase in broadening with dose (Figure 10). Rietveld refinement results are presented in Table 3. Swelling takes place linearly along both the *a*- and *c*-axis, with expansion strongly favored along the *c*-axis (Figure 11a). At a dose of 20.4×10^{18} α-events/g, *c* increases by 1.2%, compared with 0.3% along *a* (Figure 11b), making expansion along *c* four times greater than along *a*. This is similar to that noted by Rios et al. (2000a), who report about four times more swelling along *c* than *a* in natural zircon at a dose of 1.8×10^{18} α-events/g. Maximum lattice parameter swelling of ~2% along *c* and 1.5% along *a* (Holland and Gottfried 1955, Murakami et al. 1991) at a dose of 5.8×10^{18} α-events/g has been observed in zircon. In these light-particle damaged samples, a total unit cell volume swelling of up to 1.7% is seen at a dose of 20.4×10^{18} α-events/g (Figure 11c).

Discussion

Amorphization

If the 252 measured displacements associated with ^{7}Li atom and α-particle damage are partitioned according to mass, 92 atoms are displaced by the α-particle and 160 by the ^{7}Li. The total number of atoms displaced by the α-particle account for ~0.2% of the permanent atomic displacements caused by the α-particle plus recoil (Farnan and Salje 2001). These measured atomic displacement values for α-particles are in very good agreement with the predictions of the TRIM code, which predicts 78 displacements/α-track for 1.47 MeV α-particles. However, the ^{29}Si NMR signals associated with the broad peaks in Figure 8 are consistent with the partially polymerized, contiguous regions of amorphous material accumulated at the end of the particle tracks as they resemble the line shapes of the amorphized regions and not the line shapes of

broadened 'crystalline' line shapes containing isolated defects. Increasing polymerization from Q^0 (no bridging oxygen atoms, as in isolated tetrahedra) to Q^4 (all oxygen atoms bridging, as in framework silicates) increases the shielding on the Si atom and leads to more negative chemical shifts. This is reflected in the broad region at more negative chemical shifts in the damaged zircon spectra. Thus, the physical disposition of the vacancies and displaced atoms is quite different from the branching behavior of the ballistic model. This means that the defects are closely associated and are not distributed over a wide enough range to populate a significant number of unit cells and so expand the crystal lattice.

Crystalline unit cell swelling

In this study, the damaged zircon samples have not undergone significant recovery on a geological time scale. Therefore, the relative changes in *a* and *c*, which are very closely reflected in early stages of damage in natural samples (Figure 11c), must be accounted for by preferential swelling along [001] as a result of anisotropy in the expansion of the ZrO_8 dodecahedra, rather than primarily by relaxation on geological timescales. We can also compare the total lattice expansion of 1.7% with radiation damaged natural zircons where a maximum 5% unit cell volume swelling at 5.8×10^{18} α-events/g is observed (Holland and Gottfried 1955, Murakami et al. 1991). As mentioned previously, in the early stages of radiation damage in zircon (doses $<3 \times 10^{18}$ α-events/g), unit cell expansion has been attributed to localized defects caused by α-particles (Rios et al. 1999, Marples et al. 1970), while the heavy nucleus recoil creates separate isolated amorphous regions (Salje et al. 1999). The former assumption is not consistent with the unit cell volume increase of 0.21 $A^3/10^{18}$ α-events measured here compared with 3.55 $A^3/10^{18}$ α-events associated with recoil + α-particle damage in Pu-doped zircon

(Weber 1990) or 2.19 $A^3/10^{18}$ α-events associated with natural zircons (Holland and Gottfried 1955) (see Figure 11d).

One possible explanation for α-particles from the $^{10}B(n, \alpha)$ reaction not creating an equivalent amount of swelling in the crystalline fraction of these synthetic zircon samples compared with that observed in natural zircons with heavy nuclear recoil + α-damage, is that the α-tracks are of different lengths. Thus, if more defects were formed per unit α-particle track length than predicted by TRIM simulations the swelling could be accounted for. The morphology of the track is thought to be 'pearls on a string' geometry with a few isolated defects along the track and a small contiguous cascade at the end of the track (Sickafus 2008). If more defects are formed along the α-track that previously assumed, then the shorter track length of the ^{10}B α-decay would not fully represent the number of defects created by a longer U or Pu α-decay. TRIM predicts 89 displacements along the 10.7 μm track for a 4.2 MeV α-particle in $ZrSiO_4$. If the defects are distributed along the track only, with no cluster at the end of the track then ~8 defects per μm would be produced, which is a very small number of defects over many atoms. First principles electronic structure calculations of the volumetric effects of point defects in zircon (Pruneda et al. 2004, Pruneda and Artacho 2005) show that only O and Si interstitials, and the anti-site Zr_{Si}, defects would cause lattice expansion, and that to produce the magnitude of unit cell swelling (up to 5%) observed in Pu-doped samples, the number of defects would have to be on the order of 1 defect per unit cell. This would be equivalent to ~1500 defects/μm track length. This unlikely 10B (n,α) level of defect production would be counter to the current view of only a few defects being produced per micron of track length (Matzke 2007).

383 An alternative cause of the crystalline lattice swelling is that the size of the recoil cascade
384 is initially much greater than is preserved, and the rapid recrystallization of damaged regions
385 incorporates many point defects into the epitaxially recrystallized lattice which result in an
386 expanded lattice. The size of the final, relaxed cascade in zircon is calculated to be ~5 nm in
387 diameter (Trachenko et al. 2002). The amount of disruption to the crystalline lattice that is finally
388 recorded is material- and temperature-dependent. In UO_2, for example, the entire cascade
389 recrystallizes so that no observable displacement cascade is present only isolated and small
390 clusters of defects (Matzke 1992). Conversely, in zircon a large fraction of the initial damage
391 cascade is preserved.

392 Other molecular dynamics simulations of alpha recoil in zircon suggest that over half of
393 the displaced atoms in a recoil cascade recover to their original positions within a picosecond
394 (Crocombette and Ghaleb 1999, Crocombette and Ghaleb 2001). As the initial cascade relaxes
395 very quickly, it could incorporate defects which serve to swell the unit cell, which would account
396 for the higher rate of swelling in α + recoil damage compared to α-particle only.

397 The predicted number of displacements produced in a collision cascade varies greatly in
398 both experiments and simulations, and estimates usually range from ~1000 displacements
399 (Nasdala et al. 2001, Weber et al. 1998) up to 5000 (e.g. Trachenko et al. 2001, Devanathan et al.
400 2006, Farnan et al. 2007). Other studies of alpha-recoil damage have hypothesized that the size
401 of the recoil cascade is much larger than previously predicted. Studies on the $PuCoGa_5$ class of
402 plutonium superconductors showed that the superconducting transition temperatures were greatly
403 disrupted (decreased) as a result of Pu α-decay over several years, indicating a greater number of
404 initial displacements than predicted. The displacement cascade recovered entirely, with the only
405 evidence of damage being a disruption in superconducting properties (Booth et al. 2007a, Booth

et al. 2007b) by Frenkel defects. The coherence length of the Cooper pairs involved in superconductivity is very small compared to that of the long-range order probed by X-rays, making it more sensitive to disruptions in the local structure. A severe damping in the extended x-ray absorption fine structure (EXAFS) of 3-year old samples was also evidence of a high degree of local disordering, as EXAFS is another local technique sensitive to short-range disorder.

With this in mind, it is probable that the amount of recovery is sufficient to explain defects that form during epitaxial recrystallization of the damage cascade. Based on the concentration of defects required to produce the swelling observed in Pu-doped zircon samples, an additional 820 defects per recoil event would be necessary to explain experimental observations in alpha + recoil damage in crystalline fractions of zircon.

Implications

Separate effects experiments on actinide alpha radiation damage in zircon, by creating alpha particle damage without heavy daughter recoils, show that the radiation damage associated with the crystalline fraction of zircon cannot be attributed solely to the interaction with the alpha particle. The swelling of crystalline fractions of zircons damaged by alpha + recoil are significantly greater than observed here. This suggests a significant contribution to lattice expansion in the crystalline fraction of natural zircon from the rapid epitaxial recrystallization of the displacement cascade created by the heavy daughter recoil. This lattice expansion is anisotropic and similar to that created by alpha particles without recoils in samples measured within 3 years of irradiation and so occurs as an intrinsic expansion mechanism of zircon rather than as a result of relaxation along the *a*-axis on geological time scales as has been suggested

elsewhere for natural zircons.

Acknowledgments

IF acknowledges partial funding from ANSTO for a sabbatical visit. KMG acknowledges the Bill & Melinda Gates Foundation for a PhD fellowship. We are all grateful for experimental help and advice from John Hanna (ANSTO/NMR), Simon Redfern and Tony Abraham (Cambridge/XRD).

References

Ashbrook, S.E. and Farnan, I. (2004) Solid state 17O nuclear magnetic resonance spectroscopy without isotopic enrichment: direct detection of bridging oxygen in radiation damaged zircon. Solid State Nuclear Magnetic Resonance, 26, 105-112.

Babsail, L., Hamelin, N., and Townsend, P.D. (1991) Helium-ion implanted wave-guides in zircon. Nuclear Instruments and Methods in Physics Research, B59/60, 1219-1222.

Booth, C.H., Daniel, M., Wilson, R.E., Bauer, E.D., Mitchell, J.N., Moreno, N.O., Morales, L.A., Sarrao, J.L., and Allen, P.G. (2007a) Self-irradiation damage and 5f localization in $PuCoGa_5$. Journal of Alloys and Compounds, 444-445, 119-123.

Booth, C.H., Bauer, E.D., Daniel, M., Wilson, R.E., Mitchell, J.N., Morales, L.A., Sarrao, J.L., and Allen, P.G. (2007b) Quantifying structural damage from self-irradiation in a plutonium superconductor. Physical Review B, 76, 064530.

Bruno, J., and Ewing, R.C. (2006) Spent nuclear fuel. Elements, 2, 343-349.

Crocombette, J-P. and Ghaleb, D. (1999) Molecular dynamics simulation of recoil nucleus displacement cascade in zircon. In S. Zinkle, G. Lucas, R. Ewing and J. Williams, Eds., Microstructural Processes in Irradiated Materials, Vol. 540 of Materials Research Society Symposium Proceedings, 343-348, Warrendale, PA.

Crocombette, J.P. and Ghaleb, D. (2001) Molecular dynamics modeling of irradiation damage in pure and uranium-doped zircon. Journal of Nuclear Materials, 295, 167-178.

Devanathan, R., Corrales, L.R., Weber, W.J., Chartier, A., and Meis, C. (2006) Molecular dynamics simulation of energetic uranium recoil damage in zircon. Molecular Simulation, 32, 1069-1077.

Farnan, I., and Salje, E.K.H. (2001) The degree and nature of radiation damage in zircon observed by 29Si nuclear magnetic resonance. Journal of Applied Physics, 89, 2084-2090.

Farnan, I., Cho, H., and Weber, W.J. (2007) Quantification of actinide α-radiation damage in minerals and ceramics. Nature, 445, 190-193.

Geisler, T., Pidgeon, R.T., van Broswijk, W., and Pleysier, R. (2001) Kinetics of thermal recovery and recyrstallization of partially metamict zircon: a Raman spectroscopic study. European Journal of Mineralogy, 13, 1163-1176.

Gibbons, J.F. (1972) Ion implantation in semiconductors – Part II: Damage production and annealing. Proceedings of the IEEE, 60, 1062-1096.

Hedin, A. (1997) Spent nuclear fuel – how dangerous is it? SKB Technical Report 97-13,

Swedish Nuclear Fuel and Waste Management Co., 60 pp.

Holland, H., and Gottfried, D. (1955) The effect of nuclear radiation on the structure of zircon. Acta Crystallographica, 8, 291–300.

Larsen, F.H., and Farnan, I. (2002) ^{29}Si and ^{17}O (Q)CPMG-MAS solid-state NMR experiments as an optimum approach for half-integer nuclei having long T-1 relaxation times. Chemical Physics Letters, 357, 403-408.

Larson, A.C., and Von Dreele, R.B. (2004) General Structure Analysis System (GSAS*)*. Los Alamos National Laboratory Report, LAUR 86-748.

Magi, M., Lippma, E., Samoson, A., Engelhardt, A., and Grimmer, R. (1984) Solid-state high-resolution silicon-29 chemical shifts in silicates. Journal of Physics and Chemistry, 88, 1518-1522.

Marples, J.A.C., Hough, A., Mortimer, M.J., Smith, A. and Lee, J.A. (1970) Plutonium 1970 and Other Actinides. W.N. Miner, Ed., Proceedings of the Fourth International Conference on Plutonium and Other Actinides, Vol.2, 623-634, The Metallurgical Society of the American Institute of Mining, Metallurgical, and Petroleum Engineers, New York.

Marples, J.A.C. (1988) Dose rate effects in radiation damage to vitrified radioactive waste. Nuclear Instruments and Methods in Physics Research, B32, 1-4, 480-486.

Matzke, H. (1992) Radiation damage in Nuclear Materials. Nuclear Instruments and Methods in Physics Research, B65, 30-39.

Matzke, H. Radiation Effects in Nuclear Fuels. (2007) In K.E. Sickafus, E.A. Kotomin, and B.P. Uberuaga, Eds., Radiation Effects in Solids. Springer, The Netherlands, pp. 401-420.

Meldrum, A., Zinkle, S.J., and Boatner, L.A. (1999) Heavy-ion irradiation effects in the ABO_4 orthosilicates: Decomposition, amorphization, and recrystallization. Physical Review B, 59.

Murakami, T., Chakoumakos, B.C., Ewing, R.C., Lumpkin, G.R., and Weber, W.J. (1991) Alpha-decay event damage in zircon. American Mineralogist, 76, 1510-1532.

Nasdala, L., Wenzel, M., Vavra, G., Irmer, G., Wenzel, T., and Kober, B. (2001) Metamictisation of natural zircon: accumulation versus thermal annealing of radioactivity-induced damage. Contributions to Mineralogy and Petrology, 141, 125-144

Ni, Y., Hughes, J., and Mariano, A. (1995) Crystal chemistry of the monazite and xenotime structures. American Mineralogist, 80, 21-26.

Palenik, C.S., Nasdala, L., and Ewing, R.C. (2003) Radiation damage in zircon. American Mineralogist, 88, 770-781.

Pruneda, J.M., and Artacho, E. (2005) Energetics of intrinsic point defects in ZrSiO4. Physical Review B, 71, 094113.

Pruneda, J.M., Archer, T.D., and Artacho, E. (2004) Intrinsic point defects and volume swelling in ZrSiO4 under irradiation. Physical Review B, 70, 104111.

503 Rasband, W.S. (1997-2011) ImageJ. U.S. National Institutes of Health, Bethsda, Maryland,
504 USA, http://imagej.nih.gov/ij/.

505 Rietveld, H.M. (1969) A profile refinement method for nuclear and magnetic structures.
506 Journal of Applied Crystallography, 2, 65-71.

507 Rios, S., and Salje, E.K.H. (1999) Diffuse x-ray scattering from weakly metamict zircon.
508 Journal of Physics: Condensed Matter, 11, 8947-8956.

509 Rios, S., Malcherek, T., Salje, E., and Domeneghetti, C. (2000a) Localized defects in
510 radiation-damaged zircon. Acta Crystallographica Section B, 56, 947-952.

511 Rios, S., Salje, E., Zhang, M., and Ewing, R. (2000b) Amorphization in zircon: evidence for
512 direct impact damage. Journal of Physics: Condensed Matter, 12, 2401–2412.

513 Salje, E.K.H., Chrosch, J., and Ewing, R.C. (1999) Is "metamictization" of zircon a phase
514 transition? American Mineralogist, 84, 1107-1114.

515 Sickafus, K. (2008) Radiation Damage Effects in Solids. In J.D. Cossairt, V. Vylet, and J.W.
516 Edwards, Eds., Topics in Accelerator Health Physics, 246-278, Medical Physics Publishing.

517 SRIM.EXE © (1984-2010) James F. Ziegler, http://www.srim.org.

518 Trachenko, K., Dove, M., and Salje, E.K.H. (2001) Atomistic modelling of radiation damage
519 in zircon. Journal of Physics: Condensed Matter, 13, 1947-1959 (2001).

Trachenko, K., Dove, M.T. and Salje, E.K. (2002) Structural changes in zircon under a-decay irradiation. Physical Review B, 65.

Wang, L.M., and Ewing, R.C. (1992) Detailed in situ study of ion beam-induced amorphization of zircon. Nuclear Instruments and Methods in Physics Research B, 65, 324-329.

Weber, W.J. (1990) Radiation-induced defects and amorphization in zircon. Journal of Materials Research, 5, 2687-2697.

Weber, W.J. (1993) Alpha-decay-induced amorphization in complex silicate structures. Journal of the American Ceramic Society, 76, 1729-1738.

Weber, W., Ewing, R., Catlow, C., Diaz de la Rubia, T., Hobbs, L., Kinoshita, C., Matzke, H., Motta, A., Nastasi, M., Salje, E., Vance, E. and Zinkle, S. (1998) Radiation effects in crystalline ceramics for the immobilization of high-level nuclear waste and plutonium. Journal of Materials Research, 13, 1434-1484.

Weber, W.J., Ewing, R.C., and Wang, L.M. (1994) The radiation-induced crystalline-to-amorphous transition in zircon. Journal of Materials Research, 9, 688-698.

Zhang, M., Salje, E.K.H., Ewing, R.C., Farnan, I., Rios, S., Schluter, J., and Leggo, P. (2000) α-decay damage and recrystallization in zircon: Evidence for an intermediate state from infrared spectroscopy. Journal of Physics and Chemistry, 12, 5189-5199.

538 Ziegler, J.F., Biersack, J.P., and Littmark, U. (1996) The stopping and range of ions in solids.

539 Pergaman Press, New York.

540

Figure captions

Figure 1. Capture of a slow neutron by ^{10}B creates an α-particle (1.47 MeV) and ^{7}Li (0.84 MeV) which, taken together, constitute a 'light particle' event of +2.79 Mev (2.31 MeV kinetic energy).

Figure 2a. Scanning electron microscopy (SEM) image of zircon at 50 μm scale before irradiation show $ZrSiO_4$ with evenly dispersed pores (dark areas) containing boron as borosilicate or borate glass.

Figure 2b. Scanning electron microscopy (SEM) image of zircon at 6 μm scale before irradiation show $ZrSiO_4$ containing pores with 2-3 μm diameter. A minor ZrO_2 impurity (bright white spots) is also present.

Figure 3a. Image analysis of unirradiated zircon to determine the pore dimensions. A threshold is applied to create a binary image distinguishing the pore spaces from the zircon phase.

Figure 3b. Pores with an area greater than 0.005 μm are fit to ellipses, providing two measurements of the diameter.

Figure 4a. Pore radii are analyzed by producing a histogram of the pore radii from fits to ellipses.

Figure 4b. Data from the pore radii histogram are scaled for pore volume using a Jacobian transformation by multiplying the frequency of the bin by the square of the radius to account for larger pores containing more boron than smaller pores. The results are fit to a Gaussian peak profile to provide the most probable boron-containing pore radius (1.2 μm).

Figure 5a. The path of a 1.47 MeV α-particle originating from a pore and entering zircon, calculated using TRIM (Ziegler et al. 2010). The α-particle penetrates to nearly 4 μm depth, and most of the displaced atoms it produces are within the zircon structure.

Figure 5b. Comparison of the energy loss of 1.47 MeV (^{10}B(n, α)) and 4.20 MeV (from ^{238}U decay to ^{234}Th) α-particles calculated using TRIM (Ziegler et al. 2010). The path lengths are 4 μm and 11 μm for 1.47 MeV and 4.20 MeV α-particles, respectively.

Figure 6. Calibration of the ^{7}Li NMR signal intensity (central transition) produced by plotting the signal intensity against the number of ^{7}Li atoms in each spodumene calibration sample.

Figure 7. A precise measure of the dose applied to each sample is found by detection of the ^{7}Li fission product from the irradiation of ^{10}B. The ^{7}Li NMR spectrum of 28-day irradiated zircon shows an isotropic main peak from the central ½ - ½ transition and spinning sidebands from the ±3/2 - ±1/2 sattelite transitions of I = 3/2 ^{7}Li. The main peak is integrated to find dose.

587 Figure 8a. ^{29}Si NMR specta of zircons samples exposed to a range of α-particle doses from
588 unirradiated (black line) and doses of 1.0×10^{18} (green), 7.5×10^{18} (blue), and 20.5×10^{18} α-
589 events/g (red). Changes in the local structure around the silicon atoms with radiation damage
590 cause a broad peak at more negative ppm values. Relative proportions of atoms in the crystalline
591 (sharp peak) and amorphous (broadened area) regions can be found by fitting the sharp peak and
592 subtracting the area from the total integrated intensity.
593
594 Figure 8b. ^{29}Si NMR peak fitting to determine the amorphous fraction. The narrow,
595 crystalline peak at -81.6 ppm is fitted together with a Gaussian to constrain the fit. The final
596 amorphous fraction, f_a, is obtained by subtracting the area of the crystalline peak from the total
597 integral of the spectrum.
598
599 Figure 9. The amorphous fraction (in proportion of Si atoms permanently displaced) is
600 plotted against cumulative dose (in α-particles / Si atom) and fit to the direct damage equation
601 (Gibbons 1972) to provide the number of Si atoms displaced by each α-particle.
602
603 Figure 10. X-ray diffraction patterns for light-particle damaged zircon show decreasing peak
604 intensity and shift to lower 2Θ values, indicating a decrease in crystallinity and swelling of the
605 unit cell. The black pattern is undamaged, green is 1.0×10^{18} α-events/g, blue 7.5×10^{18}, and red
606 20.5×10^{18}.
607

608 Figure 11a. Change in unit cell volume for light-particle damage compared to Pu-doped and
609 natural zircon. The recoil of the heavy nucleus has a significant effect on the swelling of the
610 crystalline lattice.
611
612 Figure 11b. Increase in *a* and *c* lattice parameters with increasing dose, compared to Pu-
613 doped zircon. Red and blue diamonds are 'light-particle' and Pu-doped *a* parameters,
614 respectively, and red and blue triangles are 'light-particle' and Pu-doped *c*.
615
616 Figure 11c. Relative changes in lattice parameters *a* and *c* with increasing dose for light-
617 particle, natural, and Pu-doped zircon.
618
619 Figure 11d. Effect of α-particle damage on the unit cell volume of zircon.
620

621 **Table 1.** Calculation of the number of α-events/g in irradiated zircon samples.

Sample	^{7}Li atoms × 10^{18}	α-events/g × 10^{18}
1-day	0.28 (±0.21)	1.05 (±0.59)
10-day	1.80 (±0.23)	7.46 (±0.97)
28-day	4.32 (±0.65)	20.4 (±3.1)

622
623
624
625 **Table 2.** Amorphous fraction and the number of displacements per α-event calculated for
626 each dose using the proportion of atoms displaced found by ^{29}Si NMR.
627

Sample	Amorphous fraction f_a	Dose (α-events/Si × 10^{-3})	Displacements/ α-event
1-day	0.04 (±0.02)	0.30 (±0.25)	670 (±600)
10-day	0.09 (±0.01)	2.30 (±0.30)	240 (±50)
28-day	0.23 (±0.02)	6.30 (±0.96)	220 (±40)

628
629
630
631 **Table 3.** Increase in lattice parameters of α-particle damaged zircon with increasing dose,
632 determined by Rietveld refinement.
633

Dose (α-events/g × 10^{18})	a (Å)	c (Å)	Volume (Å^3)
0	6.60208 (±0.00016)	5.9805 (±0.00016)	260.6740 (±0.0190)
1.05 (±0.59)	6.60179 (±0.00020)	5.9841 (±0.00020)	260.809 (±0.0230)
7.46 (±0.97)	6.61062 (±0.00025)	6.00965(±0.00025)	262.623 (±0.0290)
20.4 (±3.1)	6.62488 (±0.00091)	6.03819(±0.00087)	265.01 (±0.11)

634

635 **Figure 1:**

636

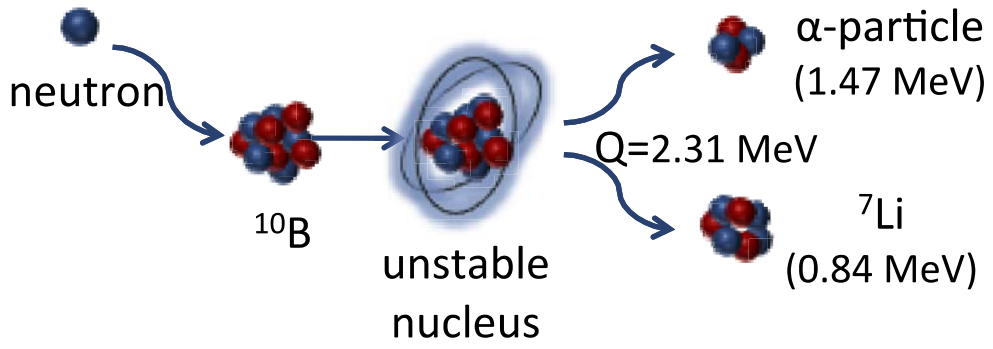

637
638

This is a preprint, the final version is subject to change, of the American Mineralogist (MSA)
Cite as Authors (Year) Title. American Mineralogist, in press.
(DOI will not work until issue is live.) DOI: http://dx.doi.org/10.2138/am.2014.4664

639

640 **Figure 2a:**

641

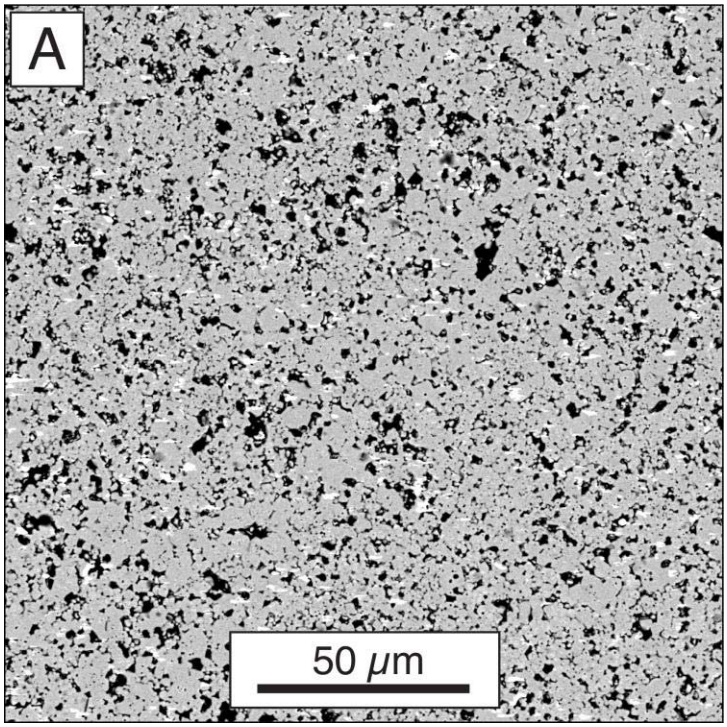

642
643

644 **Figure 2b:**

645

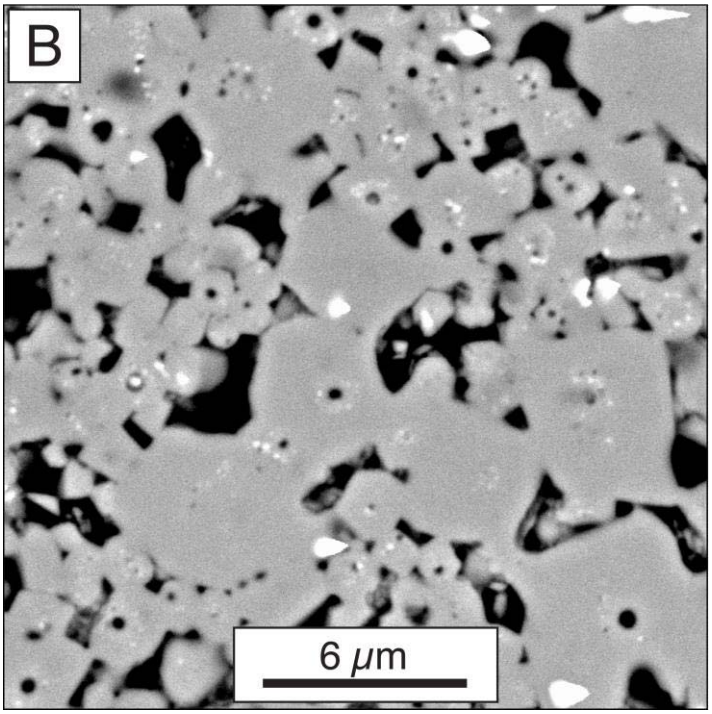

646

Figure 3a:

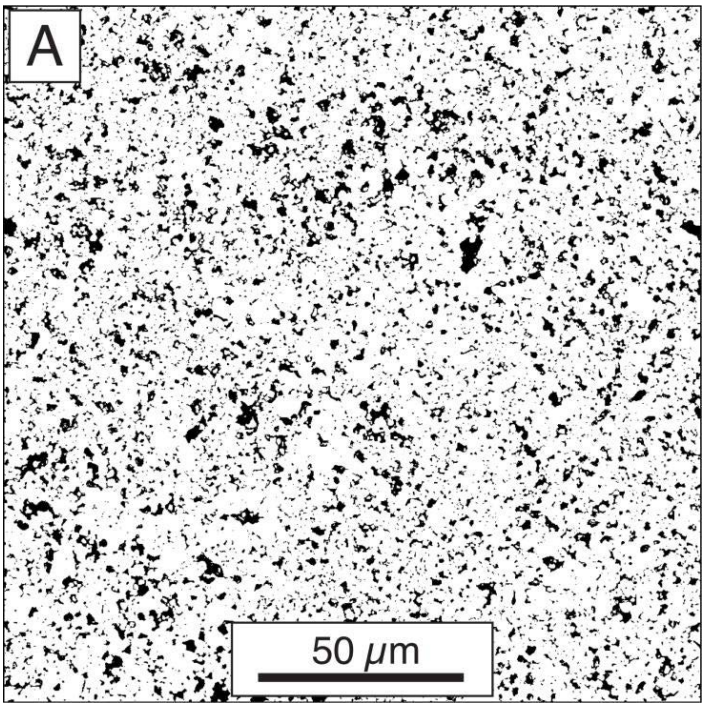

Figure 3b:

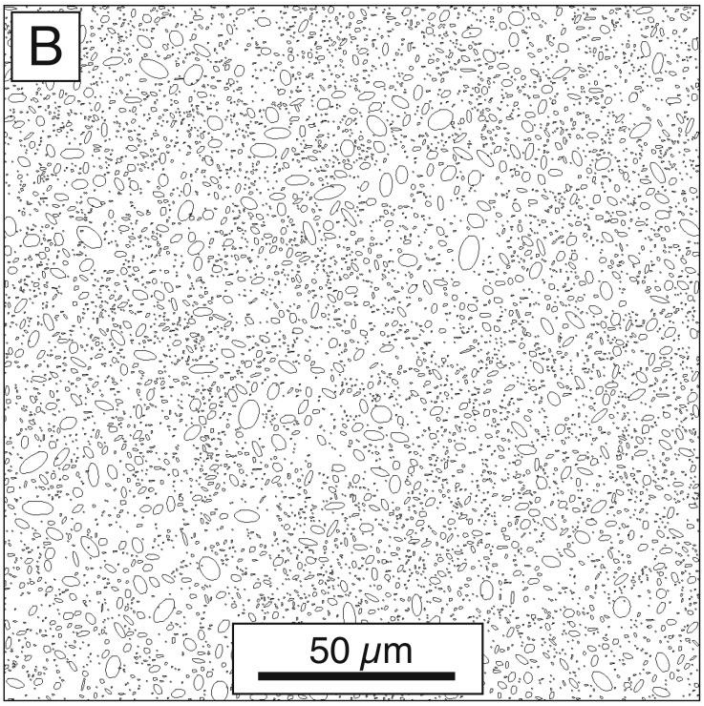

656

657 **Figure 4a:**

658

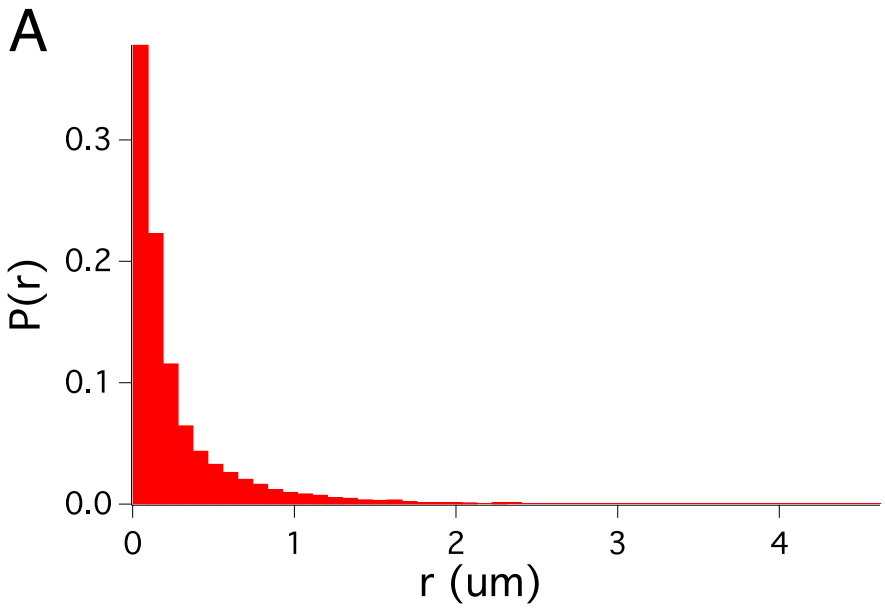

659
660
661

662 **Figure 4b:**

663

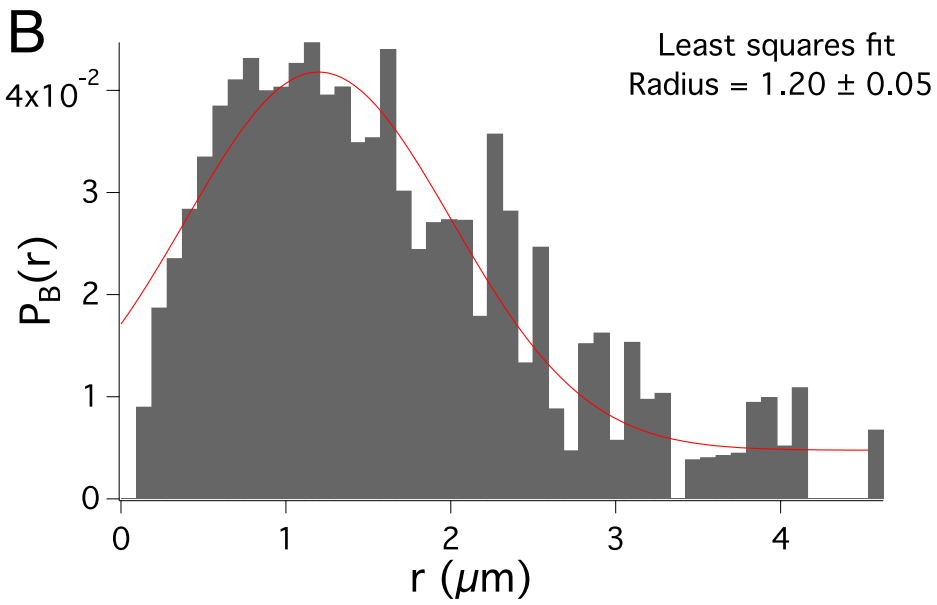

664
665

666 **Figure 5a:**

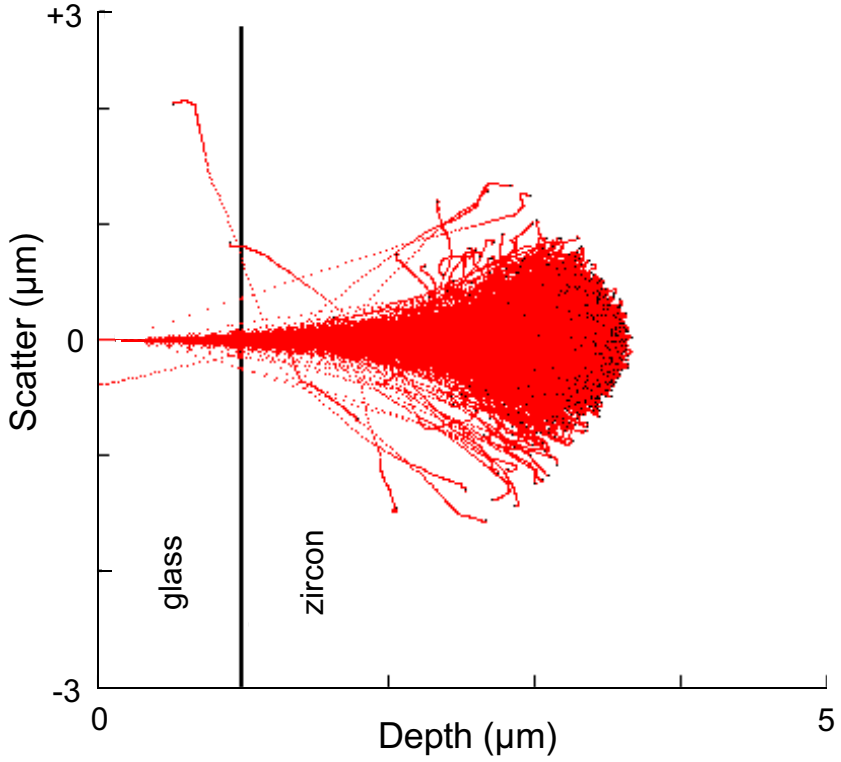

667

668 **Figure 5b:**

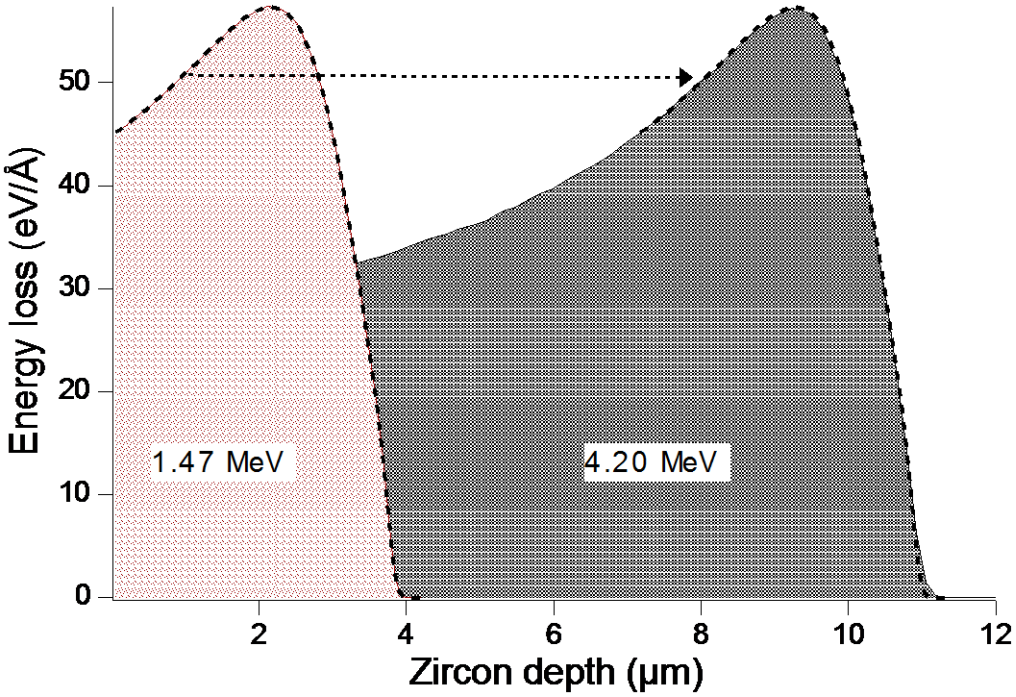

669

670

671

672 **Figure 6:**

673

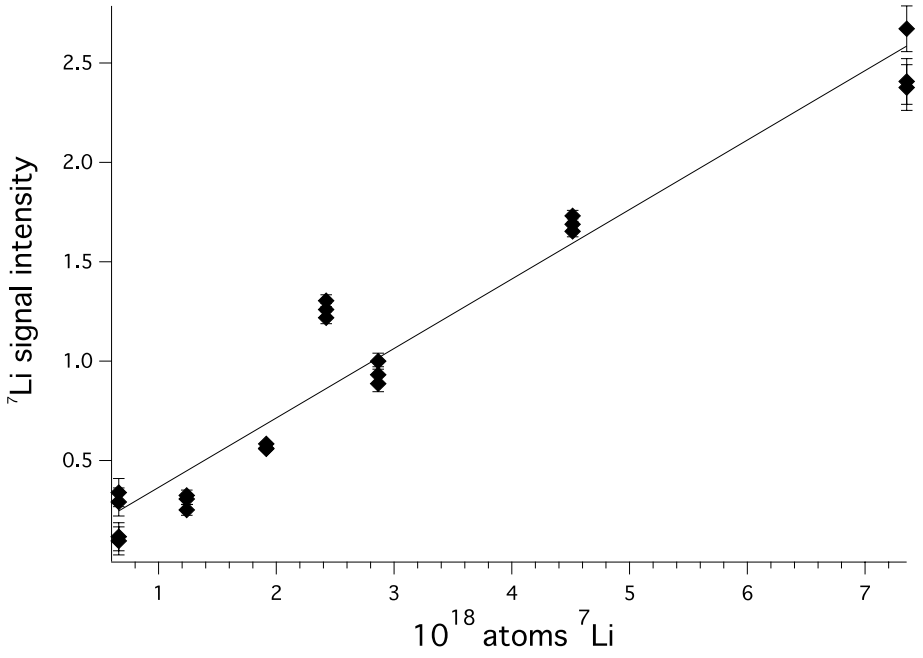

674

675

676

677

678 **Figure7:**

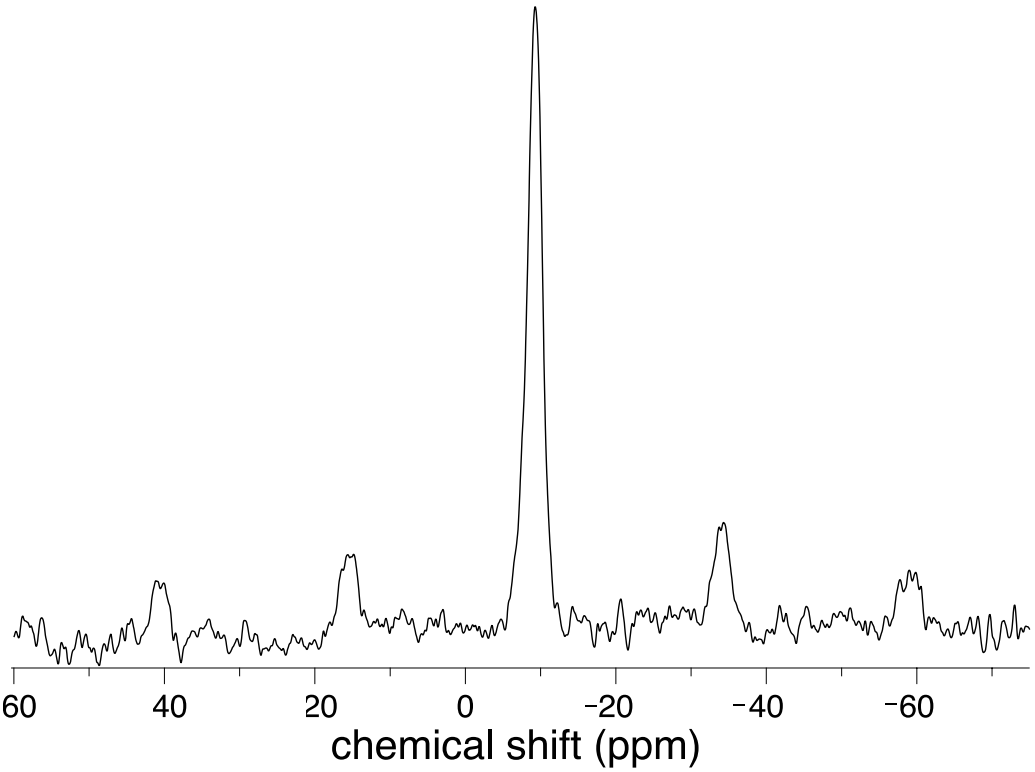

679

680

681 **Figure 8a:**

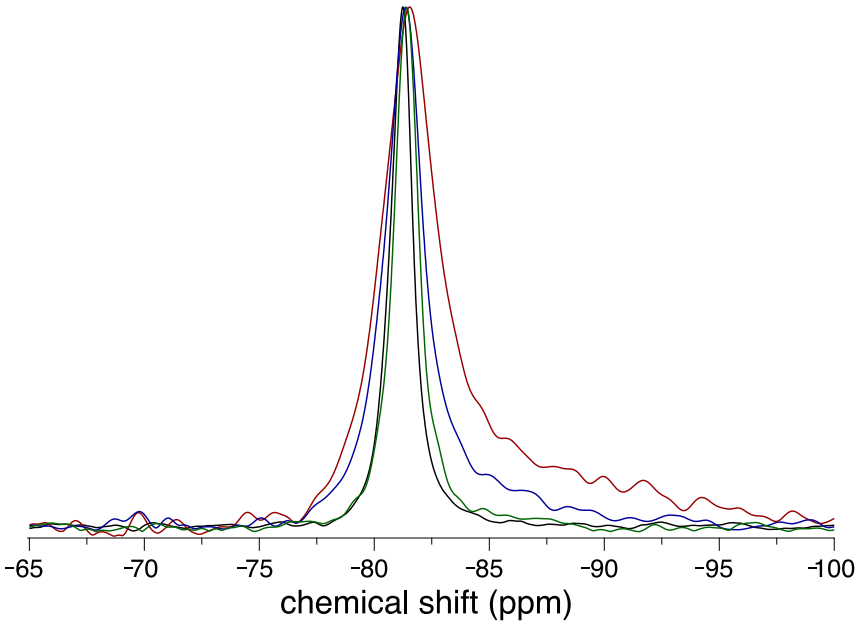

682

683

684 **Figure 8b:**

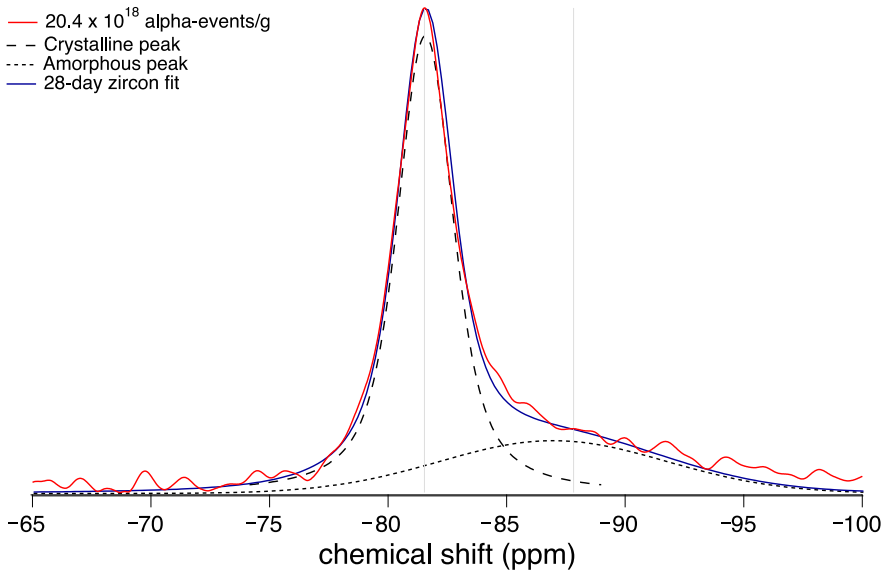

685

686

687 **Figure 9:**

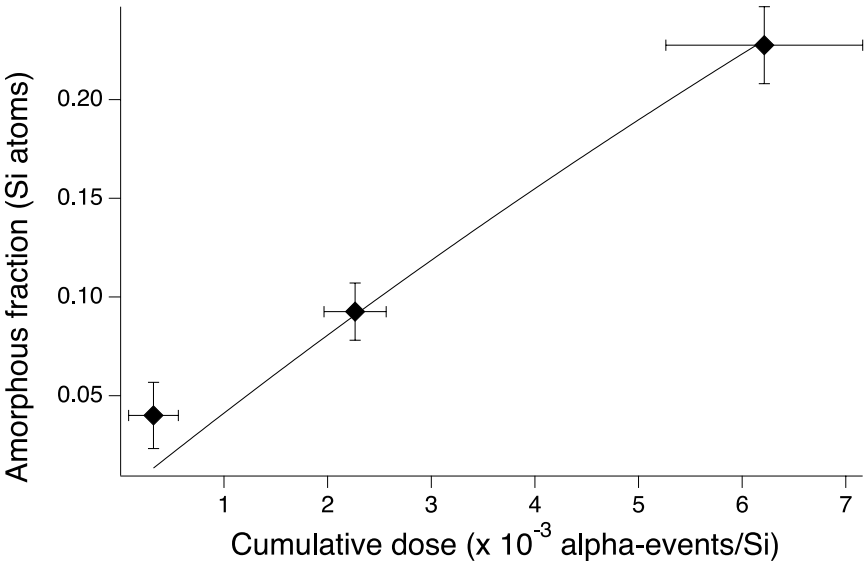

688

689 **Figure 10:**

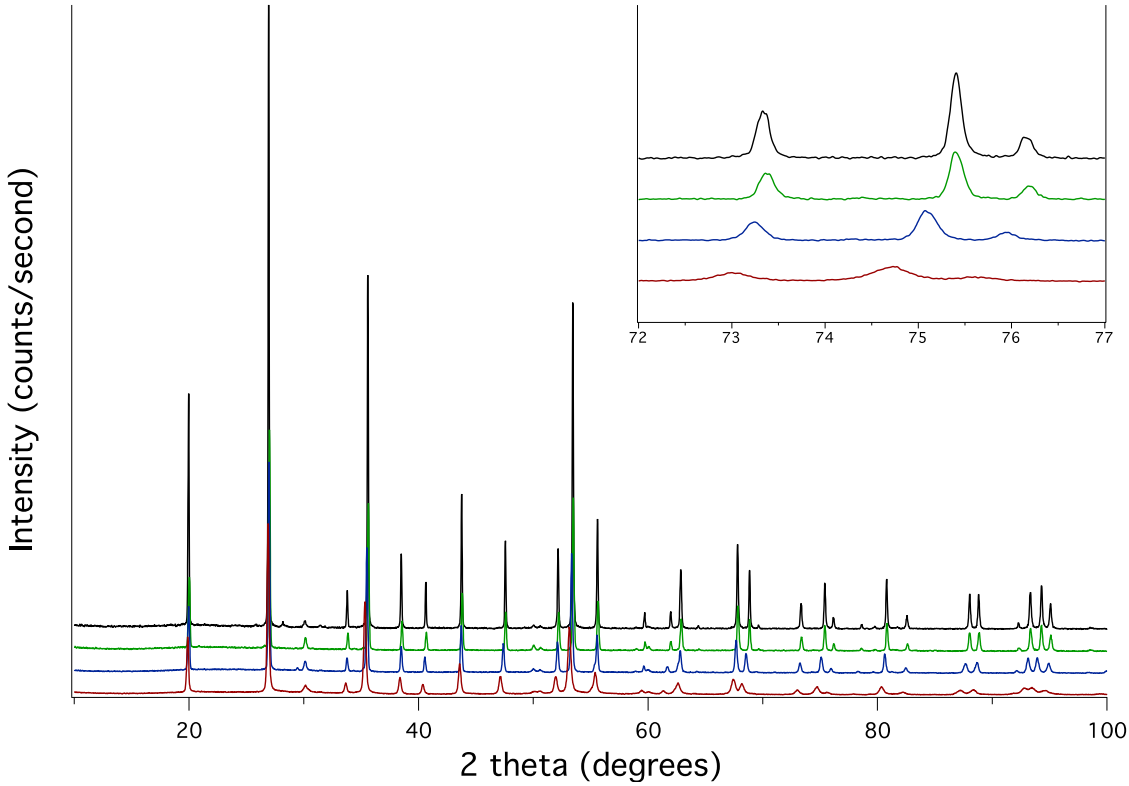

690

691 **Figure 11a:**

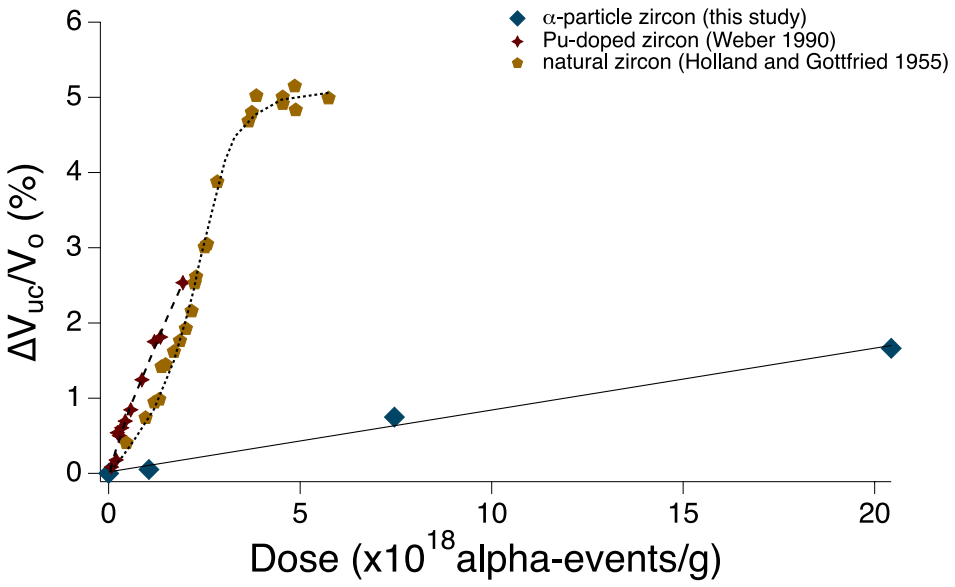

692

693 **Figure 11b:**

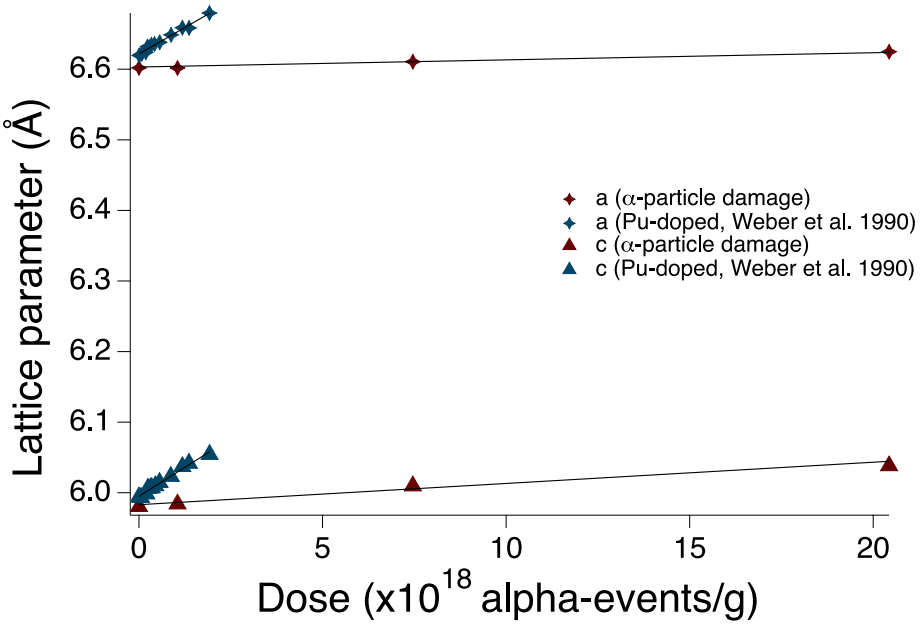

694

695

696 **Figure 11c:**

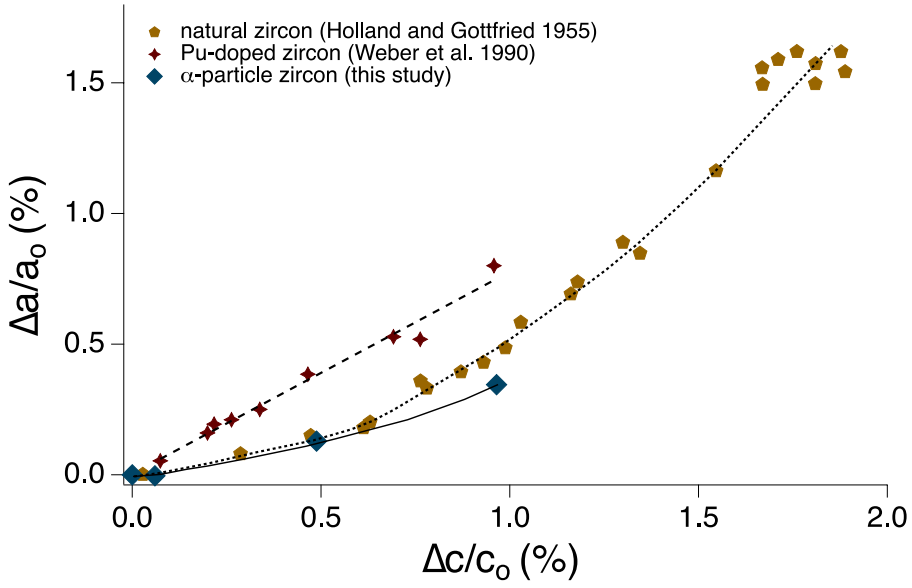

697

698 **Figure 11d:**

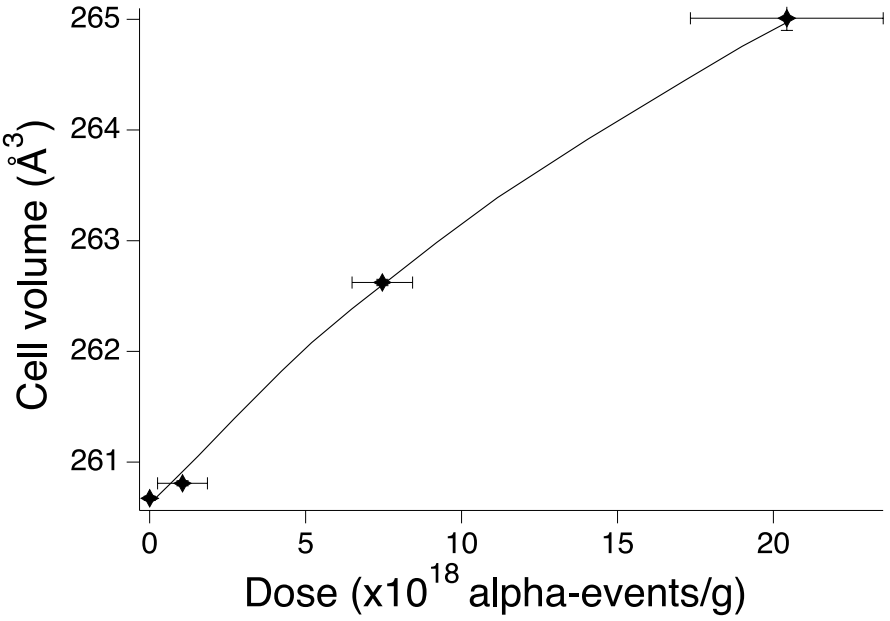

699

700